Rapid updating and improvement of airborne LIDAR DEMs through ground based SfM 3D modeling of volcanic features.

S. Kolzenburg*[1,2], M. Favalli[2], A. Fornaciai[2,3], I. Isola[2], A.J.L. Harris[4], L. Nannipieri[2], D. Giordano[1,2]

1) Dipartimento di Scienze della Terra – Università degli Studi di Torino,

Via Valperga Caluso 35, 10125 Torino, Italy

2) Istituto Nazionale di Geofisica e Vulcanologia – Sezione di Pisa,

Via della Faggiola 32, 56126 Pisa, Italy

3) Dipartimento di Fisica e Astronomia, Alma Mater Studiorum Università di Bologna

Viale Berti Pichat, 6/2, 40127 – Bologna, Italy

4) Université de Clermont-Ferrand II (Université Blaise Pascal),

Laboratoire Magmas et Vulcans, 5 Rue Kessler, 63038 Clermont-Ferrand, France

Submitted to: Transactions on Geoscience and Remote Sensing

September 2015

* Corresponding author: Stephan Kolzenburg; skolzenburg@gmail.com

Keywords: Structure from Motion (SfM), 3D surface reconstruction, LIDAR, Photogrammetry, Volcanoes, Digital Elevation Model (DEM), Lava Channel, Spatter Cone

Abstract

We present a workflow to create, scale and georeference and integrate digital elevation models (DEMs) created using open source structure from motion (SfM) multi view stereo (MVS) software into existing DEMs (derived from LIDAR data in the presented cases). The workflow also maps the root mean square error (RMSE) between the base DEM and the SfM surface model. It allows performing these tasks from the ground using consumer-grade digital cameras, open source and custom built software. We employ this workflow on three examples of different scales and morphology: 1) A scoria cone on Mt Etna, 2) A lava channel on Mauna Ulu and 3) A flank collapse scar on Mt Etna. This represents a new approach for rapid, low cost, construction- and updating of existing DEMs at high-resolution and on scales of up to several thousand square meters. We assess the self-consistency of the method by comparison of DEMs of the same feature, created from independent datasets acquired on the same day and from the same vantage points, and evaluate the effect of grid-cell-size on the reconstruction error. This method uses existing DEMs as a geo-referencing tool and can, therefore, be used in limited access and potentially hazardous areas, as it no longer relies exclusively on control targets on the ground.

1. Introduction

1.1. Surface modeling in earth science

Digital surface reconstruction plays an important role in earth sciences as an essential tool to digitize and quantify geologic processes. Among the most widespread techniques for surface reconstruction are: 1) light detection and ranging (LIDAR) (Cashman *et al.*, 2013; Favalli *et al.*, 2010; Krishnan *et al.*, 2011; Liu, 2008; Liu *et al.*, 2007); 2) classic stereo-camera photogrammetry and structure from motion (SfM), multi view stereo (MVS) photogrammetry methods (Ansan *et al.*, 2008; Favalli *et al.*, 2012; Hirano *et al.*, 2003; James and Robson, 2012; Stöcker *et al.*, 2015), and 3) radar interferometry (Farr *et al.*, 2007); see also: http://www2.jpl.nasa.gov/srtm.

LIDAR technology has been extensively used to produce DEMs of Earth and of other planets (Tarolli, 2014). LIDAR-based DEMs are commonly derived from airborne acquisition platforms (e.g. airplanes or helicopters) because they offer an optimal vantage point, a flexible geometry, and make it possible to rapidly cover large areas (Hofton *et al.*, 2006; Mazzarini *et al.*, 2007; Mouginis-Mark and Garbeil, 2005; Neri *et al.*, 2008). However, LIDAR technology is also frequently used as a ground based method, where it enables high resolution surface modeling (James *et al.*, 2009a; James and Quinton, 2014). Airborne LIDAR surveys permit generation of DEMs for large areas and recovery of detailed and comprehensive elevation maps of the covered area. Typical grid (pixel) sizes using this methodology are around 1 m (Favalli *et al.*, 2009; Krishnan *et al.*, 2011). Cashman *et al.* (2013) presented a comprehensive review of how recent advances in laser 3D surface scanning techniques have revolutionized our ability to map terrains (Harris, 2013) and to

monitor the evolution of active geologic surface features at high spatial and temporal resolutions (e.g., James et al., 2009). Cashman *et al.* (2013) describe and evaluate the application of both airborne (ALS) and terrestrial laser scanning (TLS) techniques for the interpretation of lava flow morphology as well as giving an overview over the capabilities of these techniques to output flow ages through use of relative surface roughness and surface spectral features.

The second, common, methodology for the production of 3D surface models is the classic photogrammetric approach using stereo imagery. This method requires relatively complex image acquisition, calibrating and processing techniques, and fixed geometries thus restricting the use of classical photogrammetry to well-trained experts; see for example (Duane, 1971; Faig, 1975). However, recent advances in computation technologies have allowed for the reconstruction of 3D surfaces from digital photographs taken with consumer-grade (low cost, off-the-shelf) digital cameras using the "Structure-from-Motion" (SfM) and multi view stereo photogrammetric approach (Furukawa and Ponce, 2010; James and Robson, 2014; James and Robson, 2012; Tuffen *et al.*, 2013; Westoby *et al.*, 2012; Wu, 2011). Structure-from-Motion software drastically simplifies the application of photogrammetric techniques for the non-expert user (Cecchi *et al.*, 2003; Cignoni *et al.*, 2008a; Favalli *et al.*, 2012; Fonstad *et al.*, 2013; James and Robson, 2012; Westoby *et al.*, 2012; Wu, 2011).

The third method, radar interferometry, uses phase differences in radar waves reflected from the imaged surface and returned to a sensor and is commonly used on large scales and based on satellite or aircraft platforms.

All the above methods are commonly used independently of each other and integration of data obtained from the varying methods is uncommon to date.

1.2. Use and application of LIDAR and SfM data in Volcanology.

Nowadays, large scale DEMs are largely obtained using airborne LIDAR, whereas SfM DEMs are commonly constrained to local applications (Farquharson *et al.*, 2015; James and Varley, 2012). Both methods provide ways for estimation of erupted volumes through comparison of sequential DEMs, and may be used to track temporal and spatial evolution of active lava flows, such as flow front advance and time-varying volumetric flow rate in channels. Such sequential DEM creation has already been extensively applied in volcanology, where high-precision morphometric and volumetric measurement of surface features are crucial for understanding the dynamics of for example lava flow and dome emission (Farquharson *et al.*, 2015; James and Robson, 2014; James and Varley, 2012; Mazzarini *et al.*, 2005; Tuffen *et al.*, 2013)(Favalli *et al.*, 2010) and cinder cone geometries (Fornaciai *et al.*, 2010).

Other applications of SfM in earth science spans from monitoring of riverbeds (Barker *et al.*, 1997), through estimation of erosion rates (Barker *et al.*, 1997; Daba *et al.*, 2003; Dolan *et al.*, 1978; Thomas *et al.*, 1986) to reconstructing the emplacement of highly dynamic geologic features such as active lava flows (Bretar *et al.*, 2013; Farquharson *et al.*, 2015; James *et al.*, 2009b; James and Quinton, 2014; James *et al.*, 2006). Low cost airborne applications of SfM photogrammetry are also beginning to play a role in geosciences (Hugenholtz *et al.*, 2013; Niethammer *et al.*, 2010). Recently, Johnson *et al.* (2014) has presented a case study comparing ALS, TLS and SfM approaches to map a fault line, a study

which highlighted the advantages of SfM as a simple and rapid tool to recover high quality geomorphological data.

The accuracy of DEMs derived from SfM reconstruction has been assessed by several authors (Fonstad et al., 2013; Hugenholtz et al., 2013; James and Robson, 2012). However, accuracy estimation is almost exclusively based on high-spatial resolution laser scans of the same areas or the deployment of reference points within the scene (Hugenholtz et al., 2013). All of the above described methods rely on the deployment of ground control targets or GPS-fixed control points measured in situ for scaling, georeferencing and accuracu assessment purposes (James and Robson, 2012; James et al., 2006; Westoby et al., 2012).

Both LIDAR and SfM technologies are commonly employed separately and rarely integrated for unified data treatment. This is largely due to the fact that the two methods are commonly employed from very different points of view (i.e. airborne for LIDAR and ground based for SfM) and therefore have inherently different spatial coverage.

1.3. Strengths and weaknesses of LIDAR and SfM surface modeling

Both LIDAR and SfM operate in line of sight and are, therefore, strongly affected by the deployment method and resulting vantage points. Both ground based and arial deployment modes have inherent advantages and disadvantages, independent of the surface reconstruction technique that is used. Although data acquired using airborne platforms can produce DEMs of high spatial resolution over large areas, reproduction of vertical and overhanging surface features are often problematic, resulting from its vertical viewing geometry. To reconstruct vertical and/or overhanging features requires the deployment of

6

surface based acquisition modes, such as terrestrial laser scanning or photogrammetry. Ground based data acquisition, however, has drastic limitations regarding the areal coverage since shadowing effects of objects that are not directly in line with the acquisition medium or obscured at the time of acquisition (e.g. through objects, clouds, steam etc.) are frequent. Integration of airborne and surface based data allows to overcome these difficulties and produces high resolution surface models over larger areas, as demonstrated for the SfM method by (Stöcker *et al.*, 2015).

Another disadvantage for widespread use of both airborne LIDAR, as well as TLS is that they require expert users, significant financial effort for acquisition and deployment of the device (especially ALS). In addition, although a rapid (e.g. 10s of minutes) repeat of data acquisition is possible and allows tracking the evolution of highly dynamic features at a satisfactory temporal resolution (Favalli et al., 2010), this approach is extremely expensive, mostly due to flight time costs, making rapid deployment and high frequency data collection difficult and expensive.

1.4. Integration of LIDAR and SfM data for rapid, low cost updating and improvement of existing DEMs

The spatial and temporal development of active volcanic features, such as cinder cones, collapses, growing lava flow fields and accumulating air-fall deposits, is of great interest to scientists and civil protection authorities as it yields important information about the onset, evolution and termination of potentially hazardous events. High-spatial (cm) resolution Digital Elevation Models (DEMs) generated on a regular basis (i.e. ideally on the scale of minutes to hours) are crucial for assessing the volume changes in such active volcanic areas.

Moreover, having an updated topography is essential for accurate, up-to-date, lava- and pyroclastic-flow simulation (Harris *et al.*, 2015; Tarquini and Favalli, 2010). In many places large scale DEMs are available from previous campaigns but rapidly become outdated, especially in very dynamic geologic settings such as active volcanic areas.

The hazardous, harsh, unstable and unpredictable nature of volcanic areas and eruptions calls for fast, safe and flexible remote sensing techniques. We here present a new methodology that allows for integration of existing and new surface model data. We update available airborne LIDAR data through construction and georeferencing of DEMs generated through SfM MVS and map the RMSE between thw two DEMs. We apply this methodology to volcanic features of different scales for which rapid and accurate volume change estimates are sought during and after an eruptive event to allow hazard assessment. The three targets are: 1) a scoria cone with a relatively smooth surface morphology on Mt. Etna (Italy); 2) a lava channel on the southern flanks of Mauna Ulu, Kilauea (Hawaii); and 3) the southern section of Valle del Bove, a large flank collapse feature also on Mt. Etna. The presented methodology creates high-spatial resolution DEMs that also encompass features commonly inaccessible to airborne LIDAR (e.g. overhanging and vertical walls). We integrate the two datasets to derive a complete DEM coverage with no shadow zones. We assess the quality of the derived DEM through comparison of the SfM DEM with LIDAR-derived DEMs of the same area. Using the combination of both SfM and LIDAR techniques, this methodology is able to achieve significantly increased spatial resolution and rapid updating of existing DEMs. Although previous studies have made steps towards reducing the need for ground control points (GCPs) deployed and measured in the field (Farquharson *et al.*, 2015; James and Varley, 2012; James and Robson, 2012; Tuffen *et al.*, 2013), the presented method

advances this approach by using existing DEMs for georeferencing purposes, therefore eliminating the need for field measurements. This vastly expands the capabilities of the SfM photogrammetry method so that it can be used in hazardous and inaccessible areas. The generated 3D topographic datasets are employable throughout the whole of the earth science with little financial expenditure.

2. Methodology

The approach for creating and georeferencing 3D surface models that we present here comprises five steps (see Figure 1). These are described in detail in the following sections and comprise:

1) A field campaign during which the input images are acquired;
2) Processing of the image data and creation of a 3D point cloud using Visual-SfM open source software (Furukawa *et al.*, 2010; Furukawa and Ponce, 2010; Wu, 2011, 2013);
3) Manual post-processing of the point cloud retrieved from Visual-SfM and initial user guided geospatial placing of the model using Meshlab and Scanalyze open source software developed by Cignoni *et al.* (2008a) and Pulli *et al.* (2002), respectively;
4) Accurate georeferencing through error minimization between the point cloud output and the LIDAR-derived DEM using the MINUIT minimization algorithm developed by (James and Roos, 1977); and
5) Computation of a geo-referenced DEM.

2.1. Image acquisition

Image acquisition for SfM photogrammetry does not require rigid geometries or calibration, and can be performed with any consumer-grade digital camera. For a successful reconstruction, images should be acquired from a maximum of number of different points of view that are widely distributed around the area of interest. The images used in this study were acquired at variable focal lengths using four different digital cameras: a Canon EOS 450D equipped with a canon EF-S 18-55mm f/1 3.5 5.6 IS zoom lens and a Ricoh Caplio GX100 compact camera (no changeable lense) for Monti Silvestri superiore, a Canon EOS 450D camera equipped with a Canon EF-S 18-135mm f/3.5-5.6 IS lense and a Canon G 12 compact camera for Valle del Bove on Mt. Etna, and a Pentax Optio S40 compact camera (no changeable lense) and an Canon EOS 500D camera (REBEL T1i) with a EF-S 18-55mm f/1 3.5 5.6 II zoom lense for Hawaii. The cameras were operated in automatic mode and no image optimization was performed. Distances from the imaged objects ranges from few meters (Mauna Ulu lava channel) to over 2 kilometres (far end of Valle del Bove).The image acquisition was performed during field campaigns dominantly aimed at other purposes and required little time on the ground (c.a. 1.5 h for Crateri Silvestri and Mauna Ulu; 2.5 h for Valle del Bove). Acquisition of these data did, therefore, not add significant temporal or financial effort to these field campaigns, underlining the advantages this methodology offers in terms of flexibility, data acquisition speed and financial needs. For example, the two operators in the Hawaiian case were able to acquire a total of 834 images from viewpoints spaced along either bank of a 215 m long stretch of lava channel in around 30 minutes.

10

2.2. SfM point cloud reconstruction

We use the Visual-SfM (VSfM) multicore bundle adjustment interface, an open source Structure from Motion Software developed by (Wu, 2013) in combination with the Clustering Views for Multi-view Stereo (CMVS/PMVS) code (Furukawa and Ponce, 2010). The CMVS code can operate within the VSfM shell making all processing fast and simple. The images are first loaded into the VSfM software, and automated image feature identification is performed followed by image-to-image registration using a Scale Invariant Feature Transform, SIFT (Lowe, 2004). The image feature detection and matching algorithms exploit the computing capabilities of modern Graphics Processing Units (GPUs) which allows rapid data processing. The duration of this process is dependent on the GPU's calculation capacity and the number of input images. Calculation time commonly scales exponentially with total image number and lies in the range of minutes to hours on consumer grade PC systems and seconds to minutes on multicore computers. Multicore Bundle Adjustment, (MBA) and three-dimensional sparse point cloud reconstruction, as well as CMVS/PMVS dense point cloud reconstruction, of the imaged objects is then executed within the VSfM shell. No specific lense distortion correction was applied, since all images were acquired using standard lenses without significant distortion effects. Neither were specific camera models or other parameters fixed in any way during the reconstruction process in order to assess the method's precision as a standard user without complicating the

processing workflow. The resulting dense point cloud, which is not scaled to the actual size of the object of interest, is exported by VSfM as a set of point cloud files.

2.3. Manual-cleaning and geo-placing

We impose a series of post-processing steps to the point cloud files derived from the VSfM reconstruction before final DEM creation. The following section describes the individual sub-steps and their respective functions.

2.3.1. Point Cloud Cleaning

The dense reconstruction returns point clouds with a certain number of inaccurate data points due to matching of non-correlated features (this is an inherent source of error in the reconstructions). The point cloud files also often contain data points that were reconstructed outside of the area of interest (i.e. points that lie in the background or vicinity of the object of interest). To clean the files up, we use Meshlab (Cignoni *et al.*, 2008b), a 3D mesh processing software developed at the Consiglio Nazionale delle Ricerche of Pisa, to manually restrict the point cloud to the area of interest and to remove obvious erroneous data points.

The automated reconstruction through VSfM and CMVS may also return false data-points at interfaces between the imaged object and the background. In the case of larger scale geologic features the common sources of such errors in the image are for example the border between the object and the sky in the background, large water surfaces, clouds or steam. This issue appears to be independent of the reconstruction platform (James and Robson, 2012; Westoby *et al.*, 2012). The RGB colour information for each point is available in the output

12

files from VSfM and may be used to address this issue. In this workflow we automatically remove such points based on their colour information through user-based specification of the range of colours to be removed in RGB space. This "cleaned" point cloud serves as the basis for the following steps.

2.3.2. Preparing the data for geo-referencing

The cleaned point cloud is then approximately geo-referenced in a first step by the user through definition of three points identifiable in both the base DEM and the point cloud. The user selects these points 1) on the base DEM using a GIS software of choice in our case an open source solution, (Quantum, 2013), and 2) on the point cloud using Meshlab or Scanalyze, both of which are open source 3D viewing and editing modules (Cignoni *et al.*, 2008b; Pulli *et al.*, 2002). The code developed here uses this information to scale the model and replace the relative values with the correlating absolute coordinate values for each data point.

2.3.3. Geo-referencing through RMSE minimization

The pre-cleaned and roughly geo-placed point cloud created through the SfM workflow is fed to our custom made algorithm, in combination with the LIDAR DEM to serve as the base for the final, high precision, georeferencing. To do this we use an *ad hoc* georeferencing routine based on the MINUIT minimization library developed by James and Roos (1975). In this step the algorithm reduces the root mean square error (RMSE) between the two surface models through rotating, scaling, and translation in the X, Y and Z directions.

The DEM used as the base in this geo-referencing step can, but does not have to be, identical to the DEM used for error mapping. In most cases it is preferable to mask the base DEM so as to include only those areas that are known to have had little-to-no change in topography between the time of acquisition of the new DEM and the base DEM. For example, when using this methodology to reconstruct the area of a newly emplaced lava flow, the zone where lava flows were emplaced should be masked so as to perform the geo-referencing only using areas outside of the zone of change. Failure to do so will result in placement of the new DEM below the actual surface (see Figure 6).

In some cases, after this final georeferencing step has been completed, poorly reconstructed data points become obvious and may be targeted for removal. Here the user specifies a distance margin to be excluded from the model. For each point the distance between the point position on the base DEM and the position of the point in absolute space are assessed. If the result lies outside of the distance range specified by the user, then the point is removed. RMSE minimization is then repeated.

2.4. DEM construction

The terrain models created using our SfM methodology consist of point clouds that commonly have greater point densities than LIDAR datasets. This is a result of the scale of data acquisition which in the cases presented here are obtained from a vantage point much closer to the object, and with a much greater spatial detail, than is possible with airborne laser scanning. We are, therefore, able to choose cell sizes that are significantly smaller than average cell sizes used for processing of airborne LIDAR data. This higher density of the point cloud also makes the use of interpolation methods, commonly used in areas with sparse

14

data coverage, unnecessary since in all cases presented here there were no grid cells for which no data point was available. The final DEM is then created from the point cloud after defining a grid cell size in X-Y space and averaging the Z values for all points inside each grid cell. This methodology follows standard geospatial approaches for the generation of a DEM from point cloud data, e.g. (Aguilar *et al.*, 2005; Krishnan *et al.*, 2011).

3. Case Studies

To test the methodology, we use image datasets from two volcanoes (Mt. Etna and Kilauea) and for three volcanic landforms of very different scales, morphologies and surface types. These are (Figure 2):

1) A scoria cone of relatively smooth surface morphology (Mt. Etna);
2) A lava channel on the southern flank of Mauna Ulu vent (Kilauea, Hawaii);
3) The southern section of Valle del Bove (Mt. Etna).

Figure 2 shows sample images with representative morphologies of the respective field sites. A detailed account of the area covered by the model, the number of images used, the total number of points for both LIDAR and SfM models as well as the respective point density and reconstruction error assessed through MINUIT minimization and percentage error (ratio between RMSE and average XY scale) are given in Table 1.

3.1. Etna (Monti Silvestri superiore)

This dataset comprises 885 images of the crater of a composite spatter and cinder cone built during the 1892 flank eruption of Mt. Etna. Images were acquired from the crater

rim, looking inwards into the crater from 54 points around the rim in June 2012. The cone long axis is 230 m, and the average width is 90 - 100 meters. The imaged surfaces are generally smooth and are covered with lapilli sized tephra with occasional bomb sized clasts and patches of shrubby vegetation less than 0.5 m in height and diameter. At the southern end of the central east-west elongated rim, areas of sub-vertical coherent rock faces are present, while the northern end has a small area of lava flow invasion that occurred during the 2001 flank eruption (Behncke and Neri, 2003). The LIDAR-derived DEM used for the base image was acquired in 2004 and is described in detail in Favalli *et al.* (2009). The LIDAR data was acquired using an Optech Airborne Laser Terrain Mapper (ALTM 3033); using a Class IV Laser at 1064 nanometres; the 1 sigma vertical accuracy is 0.15-0.35 m. From the LIDAR data, we extracted the Monti Silvestri crater area, which corresponds to the area of interest to be reconstructed with VSfM and which covers an area of 24,630 m^2. This area is covered by 16,343 LIDAR points resulting in a point density of 0.7 pts/m^2 (see Table 1).

3.1.1. VSfM reconstruction

The average point density of the VSfM point cloud is 534 pts/m^2, thus much greater than that of the LIDAR data (0.7 pts/m^2). After georeferencing, the RMSE difference between the SfM point cloud and the LIDAR DEM was 0.178 m. The SfM model, as well as maps of point density and surface roughness (i.e. standard deviation of all points in each respective cell relative to the averaged cell value), are shown in figure 4a-c. We also plot profiles across the DEMs derived from both methodologies. The plot of figure 4e shows a good agreement between the two datasets when viewed in a global sense. However, detailed analysis of the data highlight the ability of ground based SfM to create models of improved spatial resolution than the airborne LIDAR data (see figure 4d, plot 1 and Figure 8 for SfM accuracy

16

340 analysis), as well as the ability to resolve sub-vertical faces (see figure 4e, plot 2). The difference between the two models is assessed as RMSE for the whole area as well as by
342 calculating the local standard deviation of for each datapoint usind the following formula:

$$Standard\ deviation = \sqrt{(Lidar - SfM)^2} \quad (1)$$

344 Results are plotted along with profiles through both models for the Monto Silvestri and Hawaii examples in Figures 4 and 5, respectively. Qualitatively the differences can be seen
346 by examining the two DEMs, presented as shaded relief. The increased resolution of the image-derived SfM reconstruction becomes apparent in the reconstructions of the small lobe
348 of 2001 lava that invaded the northern floor of the Monti Silvestri crater (Fig. 3d,e). The footpaths seen in figure 3 f,g were created in the time between the two data acquisitions
350 (LIDAR and SfM) and underline the potential use of this technique for updating of existing DEM data.

352 ***3.2. Hawaii (Mauna Ulu lava channel)***

This dataset comprises a total of 834 images of a lava channel formed between the 30
354 May and 2 June 1974, being one of the final events of Kilauea's 1969-1974 Mauna Ulu eruption (Harris et al., 2009). The images were acquired from the channel levees looking into
356 the channel in September 2012. The long axis of this channel section is 215 m with a width ranging between 5 to 10 m. The imaged surfaces are generally rough and jagged with many,
358 small scale, overhanging features and intense shadowing (i.e. zones with little to no image information), representing a significant challenge for the SfM reconstruction. The LIDAR-
360 derived DEM used for georeferencing was acquired in 2009 and is available from

http://www.opentopography.org/, together with a survey report. The report states that the LIDAR data was acquired using an Optech GEMINI Airborne Laser Terrain Mapper (ALTM); using a Class IV Laser at 1047 nanometres; the 1 sigma vertical accuracy is given with 0.05-0.30 m. From this DEM, we extracted the channel area corresponding to the area of interest reconstructed with VSfM. The extracted 2,872 m^2 area was covered by 25,178 LIDAR points resulting in a LIDAR point density of 8.8 pts/m^2.

3.2.1. VSfM reconstruction

The average point density for the DEM derived from SfM reconstruction is 1,408 pts/m^2 and the RMSE between the SfM and LIDAR DEMs after georeferencing is 0.229 m. The SfM-DEM was overlain on that derived from the LIDAR data. The result is given as shaded-relief in figure 5a. There is a difference in point density between the northern (average >1,600 pts/m^2) and southern (average 400-800 pts/m^2) section of the model (Figure 5b). This is a result of the fact that significantly more image data were acquired for the northern section (657 images) than for the southern section (177 images). However, the consistency of the vertical difference between the LIDAR and SfM models (Dz) down the entire section show that this has little to no effect on the quality of the reconstruction (Fig. 5d). The plot of profiles along the central axis of the channel shows a good correlation between these two datasets (Fig. 5f). We compare the two datasets by plotting a profile down the centre axis of the channel (Figure 5e). The good correlation between the two datasets is confirmed by the fact that the elevation profiles derived from the two datasets over plot each other and the points of disagreement are highlighted by spikes in the local standard deviation. The same area has previously been studied morphologically by Harris *et al.* (2009), during which four full field days (by at least two persons) were necessary for the construction of a DEM from

kinematic GPS data for the channel levees and laser ranger measurements for the channel. The method presented here required merely a walk along the flow channel and several hours of PC processing to perform this task. This highlights the potential of SfM for rapid updating DEMs of small volcanic features.

The upper section is rougher than the lower (Figure 5e). This is consistent with the field analysis of Harris et al. (2009), which revealed that the upper section was a drained pond formed by a blockage in the channel, explaining the high point between 120 and 140 m, as well as the shallower slope to the channel floor above this level (Figure 5d).

3.3. Valle del Bove

This dataset comprises a total of 2,817 images of the inner part of the Valle del Bove, a 6.5 km × 4.5 km flank collapse feature that dominates the east flank of Etna. Images were acquired from the rim of the valley in May 2014, during the ascent up, the southern rim resulting in very low angle perspectives. The long (E-W) axis of the model is 4,500 m, and has an average (N-S) width of 2,000 m. Thus we cover the upper, south-eastern quadrant of the valley. The imaged surfaces vary between smooth slopes covered with lapilli and bomb sized tephra; vertical faces of upstanding dykes exposed by erosion in the valley walls, relatively smooth surfaced pahoehoe and rough ‘A’ā lava flow surfaces on the valley floor. The LIDAR derived DEM used as the reference base was acquired in 2010 using an Optech GEMINI Airborne Laser Terrain Mapper (ALTM); using a Class IV Laser at 1064 nanometres; the 1 sigma vertical accuracy is 0.05 - 0.30 m (INGV-database). From this we extracted the south-eastern section of Valle del Bove corresponding to the area of interest

covered by the imagery (Figure 6). This covers an area of 7,590,980 m^2 and contains 406 4,017,488 LIDAR points.

3.3.2. VSfM reconstruction

408 The scale of the modelled feature and the number of images available for the reconstruction lead to a point density of 1.4 pts/m^2. This is close to the point density of the 410 airborne LIDAR (0.5 pts/m^2). The ground based SfM data also suffers coverage problems due to the low-angle vantage point, resulting in extensive shadow zones that are not captured 412 by a sufficient number of images. There were also only a few (c.a. 6 different viewing angles; all located on the S-SW-rim of the valley) good observation points from which the 414 whole area could be imaged, resulting in difficulties in including parts of the SfM data into the unified model. However, the resulting point-cloud was sufficiently well-constrained in 416 shape to allow georeferencing to the LIDAR-derived DEM base. Where a reconstruction of data-points was possible, the two datasets show excellent agreement (Fig. 6).

418 Although poorly suited to the reconstruction of coherent models for large areas where access to a large number of vantage points is difficult, ground based SfM in combination 420 with the presented workflow allows assessment of changes in spatial features in areas where access to the area itself is difficult. We take as an example an area in the northern part of the 422 reconstructed zone which was inundated by lava flows between acquisition of the LIDAR data (2010) and the field campaign during which the images used for the SfM DEM were 424 acquired (2014). The datasets agree in zones where no lava flow inundation has occurred (Figure 6a). However, in areas where lava was emplaced between the two dates the RMSE 426 between the two models is high (between 3.5 and 10 m; see Figure 6b and enlargements in

the white boxes). The presence of a new positive topographic structure results in systematic errors when applying the presented georeferencing methodology. We therefore masked this area and re-georeferenced the data excluding the areas affected by lava flow emplacement; identified from field reports published by INGV Catania (Behncke *et al.*, 2013). This allowed us to account for the modifications in surface topography and to correct the data such that the RMSE could be reduced to 1.160 m. The absolute position and geometry of the lava flow unit(s) can be constrained with much better accuracy. Plots of profiles along and across the lava flow axis show that through masking and re-georeferencing we could produce surface models that are in good agreement with the LIDAR data outside the flow-invaded zones. This means that we can estimate lava flow thickness along and across the flow axis without the need to access the flow (Figure 6b). In this case, flow thickness ranges from 4 to 10 m and the vertical difference between the levee crest and channel infill is 0.5 to 1.5 m; with an error of ±1.1 m. (Figure 6b, profiles D and E). Misplacing of the SfM derived DEM due to changes in topography can easily be corrected if parts of the reference DEM did not change during deposition of the feature of interest (such as the periphery of the lava flow in the above example). If the topography is, however, blanketed homogenously, the post emplacement surface would be placed onto the pre deposition surface and no changes in the surface could be detected. In such cases it would be necessary to reference the SfM DEM to topographical features such as peaks or zones of steep slopes, where blanketing is not present or minimal. To further refine the data it would also be possible to include on-site measurements of the deposit thickness in a few locations to then correct the placing of the surface and allow for extraction of accurate deposit thickness data.

4. Quality Assessment and Discussion

We here perform a range of analyses to assess the accuracy and reproducibility of the models created here, as well as the effect of DEM grid size, point-cloud density and surface roughness on the quality of fit between the SfM and LIDAR models.

4.1. Reconstructions from independent image sets on the same landform

When plotted for the Monti Silvestri case, the linear arrangement of LIDAR data points, which trend NE-SE in this case (Figure 7a), becomes apparent. This is an artefact of the scanning acquisition method of airborne LIDAR, with the trend being that of the flight path and the separation being the regular sample spacing. When the vertical difference between the LIDAR and SfM DEMs is assessed it becomes clear that the LIDAR data has a large systematic error that stems from correlation and anti-correlation of the LIDAR strips. This error, here, is around 8-9 m and can be seen as NW-SE trending bands which following the LIDAR scan strips (Figure 7b).

Another systematic error apparent in the airborne LIDAR data is apparent in figure 7b. The error along the flight trajectory oscillates on a length scale of ~20 m. This may be a result of oscillation of the scanning plane of the laser, systematic vertical oscillation of the plane during the flight, or a combination of the two. An automated correction procedure, applied to the original 2004 LIDAR data, allows the reduction of the strip-to-strip root-mean-square vertical error from 0.42 to 0.15 m (Favalli *et al.*, 2009; Krishnan *et al.*, 2011), but the systematic error recovered in figure 7b remains evident. In Favalli *et al.*, (2009) a systematic error in the scanning plane was accounted for, but not the potential oscillation. Only

22

comparison with a higher-spatial resolution DEM (such as the SfM DEM presented here) highlights the presence of such systematic errors. It therefore becomes apparent, that airborne LIDAR data may not be adequate to check the accuracy of SfM DEMs and, that the resolution of airborne LIDAR data can be drastically improved using the presented method. The LIDAR data also have extensive gaps in the central parts of the craters. These gaps are filled during DEM creation by interpolation and result in an overestimation of the altitude of the points in this area.

To test the accuracy and reproducibility of the VSfM methodology and the recovered error assessments, we split the dataset into two image sub sets of the same object acquired the same day and from the same vantage points but we then processed them separately using the methodology described above. Reconstructions of Monti Silvestri were created from two datasets (M1 and M2) comprising 440 images each. Both models have an initial overabundance of image data. This allows ruling out of gross errors resulting from lack of coverage in parts of the object. The two, independently constructed, models (M1 and M2) contained 8,531,155 and 6,674,893 data points, and the average point density is 346 pts/m^2 and 271 pts/m^2, respectively. After georeferencing through MINUIT, the RMSE between the SfM and LIDAR DEMs is 0.177 m (M1) and 0.184 m (M2). Based on the above results of the analysis of the cell size effect on RMSE we have chosen a grid cell size of 0.5 m for the following comparisons.

By comparing the two, independent, surface models (Figure 7c) it is possible to assess the internal error of the SfM DEM creation methodology. Comparing the derived gridded DEMs after referencing them to the LIDAR (i.e. revealing the reproducibility of the presented

492 method) returns a minimum RMSE of 0.059 m. Comparing the SfM derived gridded DEMs after referencing them to each other (i.e. revealing the reproducibility of the SfM 494 reconstruction itself) we recover a vertical error of the presented method of min 0.037 and max 0.060 m, depending on the employed grid size (black dots in Figure 8).

496 ***4.2. The effect of grid cell size on reconstruction error***

During DEM creation, Z values of all points contained within a given X-Y grid cell are 498 averaged over the cell area. We re sampled both the LIDAR and the two SfM point cloud datasets at grid sizes of 0.1 to 3.1 m, using an incremental step of 0.1 m to investigate how 500 grid cell size affects the RMSE during georeferencing of the SfM models to the LIDAR DEMs. The results of a range of comparisons between LIDAR and SfM data are plotted in 502 figure 8. We find that:

1)When investigating the effect of changing grid size of the SfM DEM, while 504 maintaining the LIDAR DEM grid size constant at 0.5 m ; the common resolution for LIDAR derived DEMs of ETNA (Mazzarini *et al.*, 2007), we observe an initial small, but steady, 506 decrease in RMSE, for grid steps between 0.1 and 1.8 m, RMSE then remains constant around 0.229m at larger grid values(red and blue squares in Figure 8).

508 2) The RMSE between the two DEMs created by SfM and LIDAR, re-sampled at the same grid sizes (red and blue triangles) returns an initially steady error at 0.17 m until grid 510 sizes of 1.5 m. At larger grid sizes the error increases up to values of 0.190 m at a grid size of 2.8 m.

3) When comparing each point cloud with its DEM (created by averaging the point cloud elevation values over the respective grid area; red and blue diamonds) we see an expected, linear, increase in RMSE with increasing grid size. This effect increases with both increasing slope and surface roughness, since with increasing grid cell size a greater number of points is averaged over a larger area and thus, the respective distances from the averaged plane increases.

4) When comparing M1 and M2 with each other (empty black circles) the data show a significant initial decrease in RMSE with increasing grid size. It reaches a minimum of 0.060 m at the 0.6 m grid size, and then increases with increasing grid size. MINUIT error minimization through rotation, stretching and translation allows us to decrease the RMSE between the two independently created surface models to below 0.05 m (filled black circles).

The drastic difference in RMSE when comparing the two models with the LIDAR DEM, as opposed to when comparing them with each other, shows that the LIDAR data, at the acquisition scale commonly used for airborne LIDAR-DEM creation, cannot serve to assess the quality of reconstruction of the SfM-method presented here because its intrinsic error is larger than the resolution achieved with SfM.

4.3. SfM model evaluation and the effect of the viewing geometry

Here we evaluate the SfM reconstruction and the georeferencing procedure by plotting point density versus ground slope angle (Fig.9a). We also analyze the vertical difference between SfM and LIDAR models (Dz) as a function of point density, slope angle and surface roughness (Fig.9b,c,d, respectively). The results show an increasing point density

with increasing slope (Fig. 9a). This effect is a result of the viewing point from which the images were acquired in relation to the topography, with more abundant image information being acquired for slopes perpendicular to the viewing point. Thus point density is best for steeper slopes during ground based photogrammetry, and for horizontal slopes during airborne data acquisition. Dz between SfM and LIDAR DEM shows a decrease with increasing point density (Fig. 9b). This distribution reflects 1) the SfM reconstruction mechanism, where areas with an overabundance of information (high point densities) allow for higher precision of the 3D-reconstruction and 2) the georeferencing mechanism through MINUIT RMSE minimization, where high point density areas carry more weight in the minimization procedure.The RMSE reaches a plateau after an initial increase with increasing slope angle, and appears to increase again on steep slopes (Fig. 9c). This effect is a result of the geometry of the features reconstructed here, where few steep surfaces were considered. Further, these steep surfaces are prone to increased erosion resulting in a data discrepancy between the surface model of the LIDAR data acquired in 2004 (Mazzarini *et al.*, 2007) and the SfM data acquired in 2014. There is no systematic relationship between the RMSE and the model's surface roughness (Fig. 9 d), suggesting, that the surface roughness does not influence the quality of the SfM model and its georeferenciacion.

5. Conclusions

From the results reported above and the tests developed in the discussion we can draw the following conclusions:

26

1. SfM modeling combined, with the presented georeferencing methodology, allows for fast and cost-effective creation of high-spatial resolution (down to 0.1 m) DEMs for volcanic features with scales of 10s to 100s of meters.

2. The method presented here reduces the need for the deployment of georeferenced targets by using existing DEMs for georeferencing. The method, therefore, expands the capabilities of SfM photogrammetry so that it can be used more readily in hazardous and inaccessible areas. This is highlighted by the example of Valle del Bove, where lava flow invasion could be mapped from a distance of up to 2.5 kilometers.

3. SfM Photogrammetry, used in combination with the work flow presented here is an extremely flexible tool for timely DEM updates, able to update DEMs on an daily basis to allow tracking of cm-scale surface changes. It thus can be applied in dynamic environments to, for example, assess volumetric changes of volcanic features over time, whether that be cone growth, air fall build up or lava flow emplacement. Further, DEM-to-DEM subtraction allows mass flux rates to be obtained at a precision hitherto impossible.

4. Ground based deployment of the method presented in this manuscript does not produce a coherent DEM for large (km-scale) areas. However, while the absolute RMSE increases with increasing area of coverage, the percentage error remains constant and low (below 0.118 for the Mt Etna examples and 0.427 for Mauna Ulu). Thus the presented integration of existing and SfM derived DEMs can nonetheless be

of great value for rapid assessment of, for example, the thickness, area and volume of newly emplaced lava flows, pyroclastic flows or air-fall deposits.

Acknowledgements

We would like to thank Daniele Andronico and Mauro Coltelli from INGV Catania for their support during a field campaign on Mt Etna during which part of the dataset for the Valle del Bove reconstruction was acquired. We acknowledge IT support from Giorgio Carbotta (UniTo). This research was partially funded by an EX60% project under the "ricerca locale dell'Univeristà di Torino (2012); titled: "Studio integrato di terrreno, laboratorio ed analisi remote sensing per l'implementazione di modelli reologici per la messa in posto di flussi lavici basso-viscosi in aree vulcaniche attive". Stephan Kolzenburg acknowledges an Compagnia San Paulo doctoral scholarship for financial support. Alessandro Fornaciai has carried out this work in the frame of Dottorato di Geofisica, Dipartimento di Fisica e Astronomia, Alma Mater Studiorum Università di Bologna. This paper benefitted from the constructive comments of Mike James, Felix von Aulock and an anonymous reviewer, as well as the editor Antonio Plaza.

9. References

Aguilar, F.J., Agüera, F., Aguilar, M.A., Carvajal, F., 2005. Effects of terrain morphology, sampling density, and interpolation methods on grid DEM accuracy. Photogrammetric Engineering & Remote Sensing 71, 805-816.

Ansan, V., Mangold, N., Masson, P., Gailhardis, E., Neukum, G., 2008. Topography of valley networks on Mars from Mars Express High Resolution Stereo Camera digital elevation models. Journal of Geophysical Research: Planets (1991–2012) 113.

Barker, R., Dixon, L., Hooke, J., 1997. Use of terrestrial photogrammetry for monitoring and measuring bank erosion. Earth Surface Processes and Landforms 22, 1217-1227.

Behncke, B., De Beni, E., Proietti, C., 2013. Misure GPS del nuovo cono di scorie del Cratere di SE, Etna

Aggiornamento del 03 maggio 2013. INGV Catania, INGV Catania.

Behncke, B., Neri, M., 2003. The July–August 2001 eruption of Mt. Etna (Sicily). Bulletin of Volcanology 65, 461-476.

Bretar, F., Arab-Sedze, M., Champion, J., Pierrot-Deseilligny, M., Heggy, E., Jacquemoud, S., 2013. An advanced photogrammetric method to measure surface roughness: Application to volcanic terrains in the Piton de la Fournaise, Reunion Island. Remote Sensing of Environment 135, 1-11.

Cashman, K., Soule, S., Mackey, B., Deligne, N., Deardorff, N., Dietterich, H., 2013. How lava flows: New insights from applications of lidar technologies to lava flow studies. Geosphere 9, 1664-1680.

Cecchi, E., van Wyk de Vries, B., Lavest, J.-M., Harris, A., Davies, M., 2003. n-view reconstruction: a new method for morphological modelling and deformation measurement in volcanology. Journal of Volcanology and Geothermal Research 123, 181-201.

Cignoni, P., Corsini, M., Dellepiane, M., Ranzuglia, G., Vergauven, M., Van Gool, L., 2008a. Meshlab and Arc3D: Photo-reconstruction and processing 3D meshes, Open Digital Cultural Heritage Systems Conference, p. 61.

Cignoni, P., Corsini, M., Ranzuglia, G., 2008b. Meshlab: an open-source 3d mesh processing system. Ercim news 73, 45-46.

Daba, S., Rieger, W., Strauss, P., 2003. Assessment of gully erosion in eastern Ethiopia using photogrammetric techniques. Catena 50, 273-291.

Dolan, R., Hayden, B., Heywood, J., 1978. A new photogrammetric method for determining shoreline erosion. Coastal Engineering 2, 21-39.

Duane, C.B., 1971. Close-range camera calibration. Photogrammetric engineering 37, 855-866.

Faig, W., 1975. Calibration of close-range photogrammetric systems: Mathematical formulation. Photogrammetric engineering and remote sensing 41.

Farquharson, J., James, M., Tuffen, H., 2015. Examining rhyolite lava flow dynamics through photo-based 3D reconstructions of the 2011–2012 lava flowfield at Cordón-Caulle, Chile. Journal of Volcanology and Geothermal Research 304, 336-348.

Farr, T.G., Rosen, P.A., Caro, E., Crippen, R., Duren, R., Hensley, S., Kobrick, M., Paller, M., Rodriguez, E., Roth, L., 2007. The shuttle radar topography mission. Reviews of geophysics 45.

Favalli, M., Fornaciai, A., Isola, I., Tarquini, S., Nannipieri, L., 2012. Multiview 3D reconstruction in geosciences. Computers & Geosciences 44, 168-176.

Favalli, M., Fornaciai, A., Mazzarini, F., Harris, A., Neri, M., Behncke, B., Pareschi, M.T., Tarquini, S., Boschi, E., 2010. Evolution of an active lava flow field using a multitemporal LIDAR acquisition. Journal of Geophysical Research: Solid Earth (1978–2012) 115.

Favalli, M., Fornaciai, A., Pareschi, M.T., 2009. LIDAR strip adjustment: application to volcanic areas. Geomorphology 111, 123-135.

Fonstad, M.A., Dietrich, J.T., Courville, B.C., Jensen, J.L., Carbonneau, P.E., 2013. Topographic structure from motion: a new development in photogrammetric measurement. Earth Surface Processes and Landforms 38, 421-430.

Fornaciai, A., Behncke, B., Favalli, M., Neri, M., Tarquini, S., Boschi, E., 2010. Detecting short-term evolution of Etnean scoria cones: a LIDAR-based approach. Bulletin of Volcanology 72, 1209-1222.

Furukawa, Y., Curless, B., Seitz, S.M., Szeliski, R., 2010. Towards internet-scale multi-view stereo, 2010 IEEE Conference on Computer Vision and Pattern Recognition (CVPR). IEEE, pp. 1434-1441.

Furukawa, Y., Ponce, J., 2010. Accurate, dense, and robust multiview stereopsis. IEEE Transactions on Pattern Analysis and Machine Intelligence 32, 1362-1376.

Harris, A., 2013. Thermal Remote Sensing of Active Volcanoes: A User's Manual. Cambridge University Press.

Harris, A.J., Favalli, M., Mazzarini, F., Hamilton, C.W., 2009. Construction dynamics of a lava channel. Bulletin of Volcanology 71, 459-474.

Harris, A.J., Rhéty, M., Gurioli, L., Villeneuve, N., Paris, R., 2015. Simulating the thermorheological evolution of channel-contained lava: FLOWGO and its implementation in EXCEL. Geological Society, London, Special Publications 426, SP426. 429.

Hirano, A., Welch, R., Lang, H., 2003. Mapping from ASTER stereo image data: DEM validation and accuracy assessment. ISPRS Journal of Photogrammetry and Remote Sensing 57, 356-370.

Hofton, M.A., Malavassi, E., Blair, J.B., 2006. Quantifying recent pyroclastic and lava flows at Arenal Volcano, Costa Rica, using medium-footprint lidar. Geophysical Research Letters 33, n/a-n/a.

Hugenholtz, C.H., Whitehead, K., Brown, O.W., Barchyn, T.E., Moorman, B.J., LeClair, A., Riddell, K., Hamilton, T., 2013. Geomorphological mapping with a small unmanned aircraft system (sUAS): Feature detection and accuracy assessment of a photogrammetrically-derived digital terrain model. Geomorphology 194, 16-24.

James, F., Roos, M., 1975. Minuit-a system for function minimization and analysis of the parameter errors and correlations. Computer Physics Communications 10, 343-367.

James, F., Roos, M., 1977. MINUIT, CERN program library entry D506.

James, M., Robson, S., 2014. Sequential digital elevation models of active lava flows from ground-based stereo time-lapse imagery. ISPRS Journal of Photogrammetry and Remote Sensing 97, 160-170.

James, M., Varley, N., 2012. Identification of structural controls in an active lava dome with high resolution DEMs: Volcán de Colima, Mexico. Geophysical Research Letters 39.

James, M.R., Pinkerton, H., Applegarth, L.J., 2009a. Detecting the development of active lava flow fields with a very-long-range terrestrial laser scanner and thermal imagery. J. Geophys. Res. 36, L22305.

James, M.R., Pinkerton, H., Applegarth, L.J., 2009b. Detecting the development of active lava flow fields with a very□long□range terrestrial laser scanner and thermal imagery. Geophysical Research Letters 36.

James, M.R., Quinton, J.N., 2014. Ultra-rapid topographic surveying for complex environments: the hand-held mobile laser scanner (HMLS). Earth Surface Processes and Landforms 39, 138-142.

James, M.R., Robson, S., 2012. Straightforward reconstruction of 3D surfaces and topography with a camera: Accuracy and geoscience application. J. Geophys. Res.: Earth Surface 117, F03017.

James, M.R., Robson, S., Pinkerton, H., Ball, M., 2006. Oblique photogrammetry with visible and thermal images of active lava flows. Bulletin of Volcanology 69, 105-108.

Johnson, K., Nissen, E., Saripalli, S., Arrowsmith, J.R., McGarey, P., Scharer, K., Williams, P., Blisniuk, K., 2014. Rapid mapping of ultrafine fault zone topography with structure from motion. Geosphere 10, 969-986.

Krishnan, S., Crosby, C., Nandigam, V., Phan, M., Cowart, C., Baru, C., Arrowsmith, R., 2011. OpenTopography: a services oriented architecture for community access to LIDAR topography, Proceedings of the 2nd International Conference on Computing for Geospatial Research & Applications. ACM, p. 7.

Liu, X., 2008. Airborne LiDAR for DEM generation: some critical issues. Progress in Physical Geography 32, 31-49.

Liu, X., Zhang, Z., Peterson, J., Chandra, S., 2007. LiDAR-derived high quality ground control information and DEM for image orthorectification. GeoInformatica 11, 37-53.

Lowe, D.G., 2004. Distinctive image features from scale-invariant keypoints. International journal of computer vision 60, 91-110.

Mazzarini, F., Pareschi, M.T., Favalli, M., Isola, I., Tarquini, S., Boschi, E., 2005. Morphology of basaltic lava channels during the Mt. Etna September 2004 eruption from airborne laser altimeter data. Geophysical Research Letters 32.

Mazzarini, F., Pareschi, M.T., Favalli, M., Isola, I., Tarquini, S., Boschi, E., 2007. Lava flow identification and aging by means of lidar intensity: Mount Etna case. Journal of Geophysical Research: Solid Earth (1978–2012) 112.

712 Mouginis-Mark, P.J., Garbeil, H., 2005. Quality of TOPSAR topographic data for volcanology studies at Kilauea Volcano, Hawaii: An assessment using airborne lidar
714 data. Remote Sensing of Environment 96, 149-164.

Neri, M., Mazzarini, F., Tarquini, S., Bisson, M., Isola, I., Behncke, B., Pareschi, M.T., 2008.
716 The changing face of Mount Etna's summit area documented with Lidar technology. Geophysical Research Letters 35, n/a-n/a.

718 Niethammer, U., Rothmund, S., James, M., Travelletti, J., Joswig, M., 2010. UAV-based remote sensing of landslides. International Archives of Photogrammetry, Remote
720 Sensing and Spatial Information Sciences 38, 496-501.

Pulli, K., Curless, B., Ginzton, M., Rusinkiewicz, S., Pereira, L., Wood, D., 2002. Scanalyze
722 v1. 0.3: A computer program for aligning and merging range data. Stanford Computer Graphics Laboratory Stanford.

724 Quantum, G., 2013. Development Team, 2012. Quantum GIS Geographic Information System. Open Source Geospatial Foundation Project. Free Software Foundation,
726 India.

Stöcker, C., Eltner, A., Karrasch, P., 2015. Measuring gullies by synergetic application of
728 UAV and close range photogrammetry — A case study from Andalusia, Spain. Catena 132, 1-11.

730 Tarolli, P., 2014. High-resolution topography for understanding Earth surface processes: Opportunities and challenges. Geomorphology 216, 295-312.

732 Tarquini, S., Favalli, M., 2010. Changes of the susceptibility to lava flow invasion induced by morphological modifications of an active volcano: the case of Mount Etna, Italy.
734 Natural hazards 54, 537-546.

Thomas, A., Welch, R., Jordan, T., 1986. Quantifying concentrated-flow erosion on cropland
736 with aerial photogrammetry. Journal of Soil and Water Conservation 41, 249-252.

Tuffen, H., James, M., Castro, J., Schipper, C., 2013. Exceptional mobility of a rhyolitic
738 obsidian flow: observations from Cordón Caulle, Chile, 2011–2013. Nature Comm 2709.

740 Westoby, M., Brasington, J., Glasser, N., Hambrey, M., Reynolds, J., 2012. 'Structure-from-Motion'photogrammetry: A low-cost, effective tool for geoscience applications.
742 Geomorphology 179, 300-314.

Wu, C., 2011. VisualSFM: A visual structure from motion system.

744 Wu, C., 2013. Towards linear-time incremental structure from motion, 3DTV-Conference, 2013 International Conference on. IEEE, pp. 127-134.

746

Figure Captions

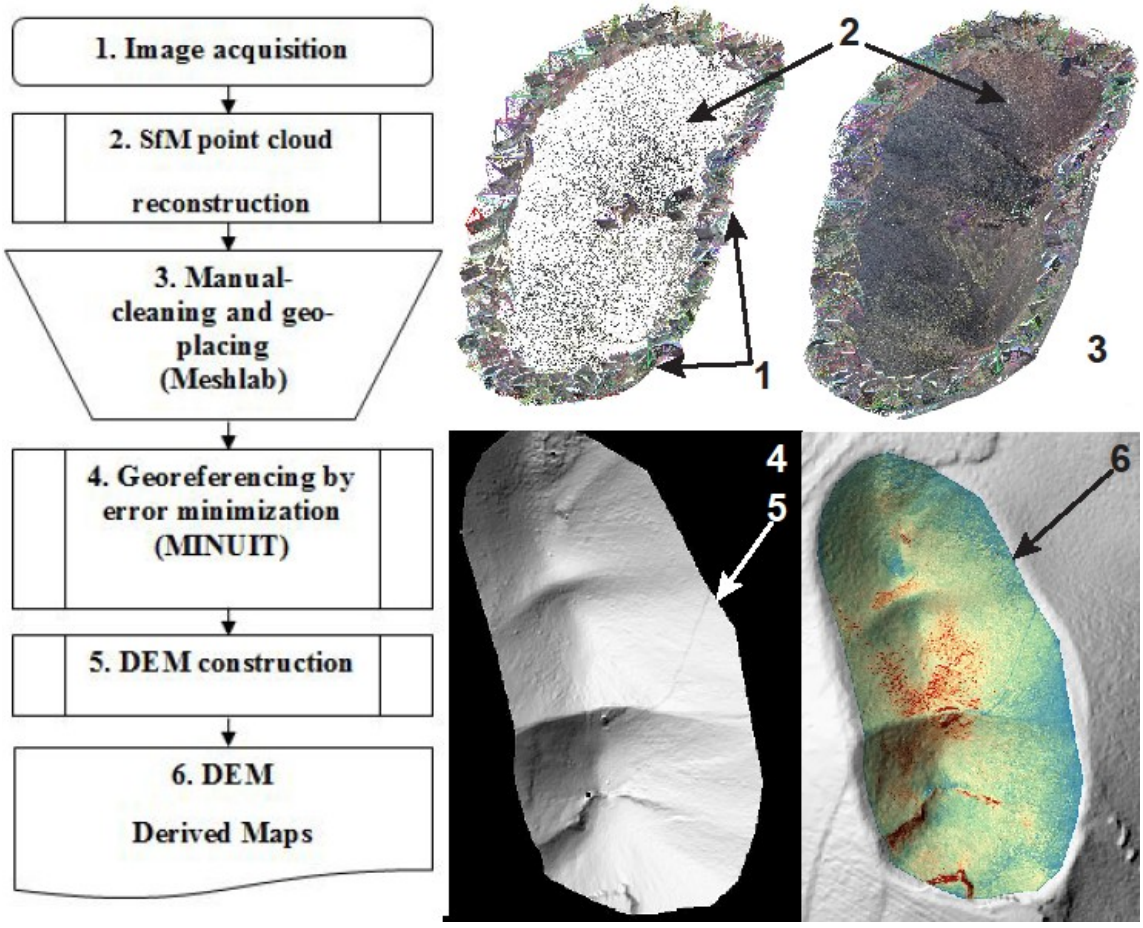

Figure 1: Schematic of data processing work flow.

Flow diagram describing the individual data processing steps. Samples of the products of steps 1 through 6 are shown in the four graphics on the right and labelled respectively.

Figure 2: Field site characterization:

Sample pictures showing characteristic features of the respective field sites: a), Monti Silvestri superiore; tephra cones on Mt Etna featuring rather smooth surfaces and gentle slopes. Model length and width c.a. 230 m and 135 m, respectively. b) Lava channel on Mauna Ulu, Hawaii, model dimensions c.a. 200 m length and 10 m width, featuring (in relation to the model scale) jagged *ʻAʻā*-flow surfaces. Channel width c.a. 10 m. c) Valle del Bove, model diameter c.a. 4.5 km, a large valley resulting from a flank collapse on the eastern slopes of Mt Etna featuring steep side walls comprising volcaniclastic and lava flow strata and a relatively smooth (in relation to the overall scale of the model) valley floor that is covered with several generations of dominantly A'a-type lava flows. The valley width is c.a. 5 km.

34

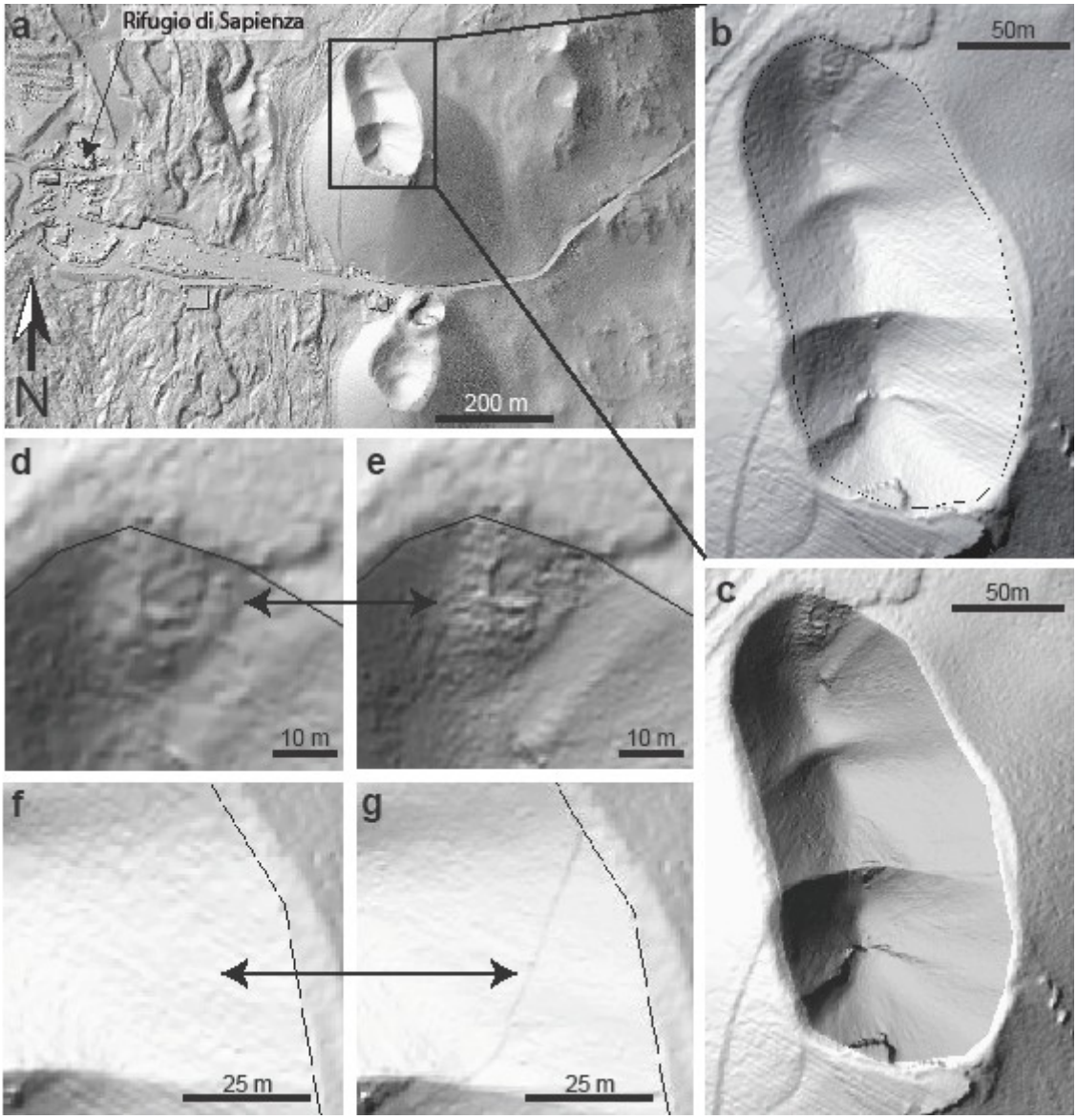

772

774**Figure 3: Comparison of Monti Silvestri LIDAR and SfM DEMs rendered as hill shade.**

776a) Overview of the study area located on the slopes of Mt Etna in close vicinity to the Rifugio di Sapienza. The landform "Monti Silvestri superiore" is the elongated composite crater in 778the black box. b) Zoom in to the LIDAR data of "Cono Doppio"; note the NW-SE trending linear artefacts resulting from errors in the airborne laser scanning. The black contour defines 780the outer boundary of the study area for the comparison between LIDAR and SfM data c) Hillshade map created from the DEM data generated using the SfM-workflow presented in 782this manuscript. Note that the SfM data is only displayed for the inside of the landform outlined by the black contour. d+e). Comparison of the DEMs generated from LIDAR and 784SfM data, respectively. The excerpts show the 2002 lava flow inundating the north end of the Monti Silvestri superiore landform. Note the significantly enhanced detail in resolution in the 786DEM generated from SfM data. f+g) Detail of the internal, eastern flanks of Monti Silvestri superiore; Hill shaded visualization of the DEM data created using LIDAR and SfM,

788 respectively. The line trending NE-SW is a footpath of c.a. 1 m width that is barely visible in
the LIDAR data whereas in the SfM data it can be seen in great detail.
790

36

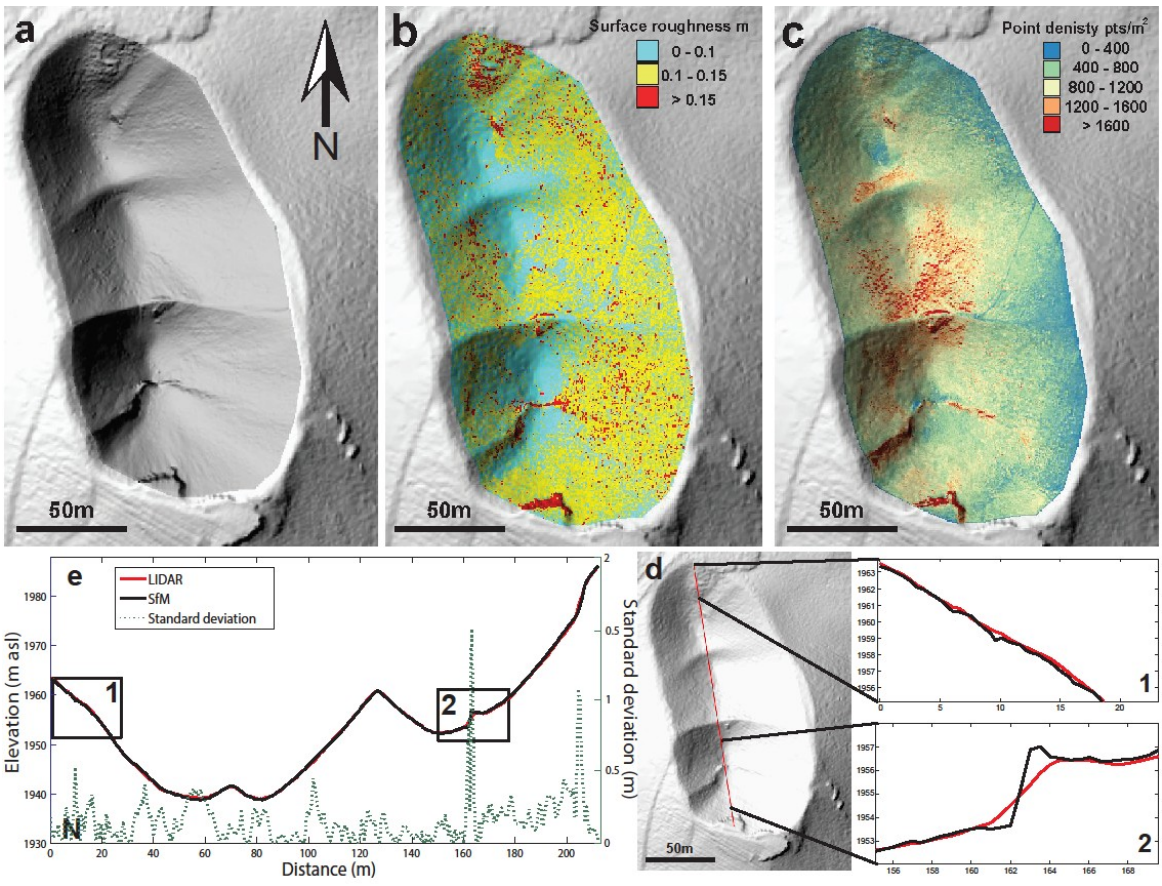

Figure 4: Evaluation of the SfM DEM Monti Silverstri.

a) Hillshaded DEM generated through the workflow presented here. The study area (dark grey) is overlain on the LIDAR DEM b) Surface roughness of the SfM DEM (i.e. standard deviation of all points in each respective cell relative to the averaged cell value) c) Point density of the SfM model in points per square meter. d) Profiles from North to South along the red line in the map. LIDAR data is displayed in red, SfM data in black. The standard deviation for each profile point calculated using formula (1) is plotted as the dashed line. The two datasets show good agreement on the larger scale. Squares 1 and 2 are enlarged as subplots and show the superior resolution of the SfM DEM at smaller scale, also evidenced by the spikes in local standard deviation. The SfM DEM is able to reproduce a more detailed surface, where the LIDAR data smooth the surface. Subplot 2 highlights this aspect, as the LIDAR data fails to reproduce the sub vertical section of the profile. d) Entire profile from North to South along the red line in the map.

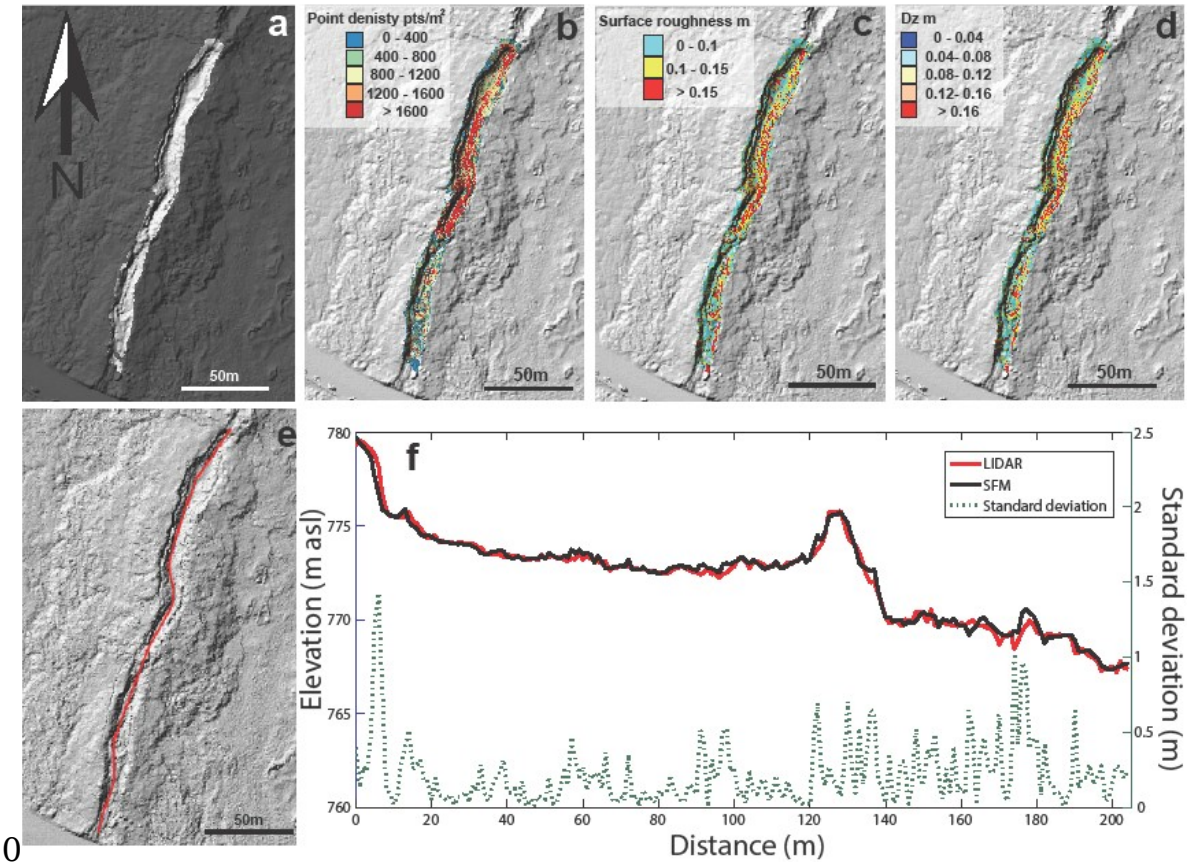

Figure 5: Evaluation of the SfM DEM Mauna Ulu.

a) Hillshaded DEM generated through the workflow presented here. The study area (light grey) is overlain on the LIDAR DEM. b) Point density of the SfM model in points per square meter. c) Surface roughness of the SfM DEM (i.e. standard deviation of all points in each respective cell relative to the averaged cell value) d) Vertical distance (Dz) between the SfM and the LIDAR DEM. e) map showing the location of the profile line f) Profile from North to South along the red line in map (e) for both LIDAR and SfM data. Note the good agreement of the two datasets created using completely different methods. The local standard deviation increases in the lower part of the lava channel as a result of the rougher lava surface in this area.

38

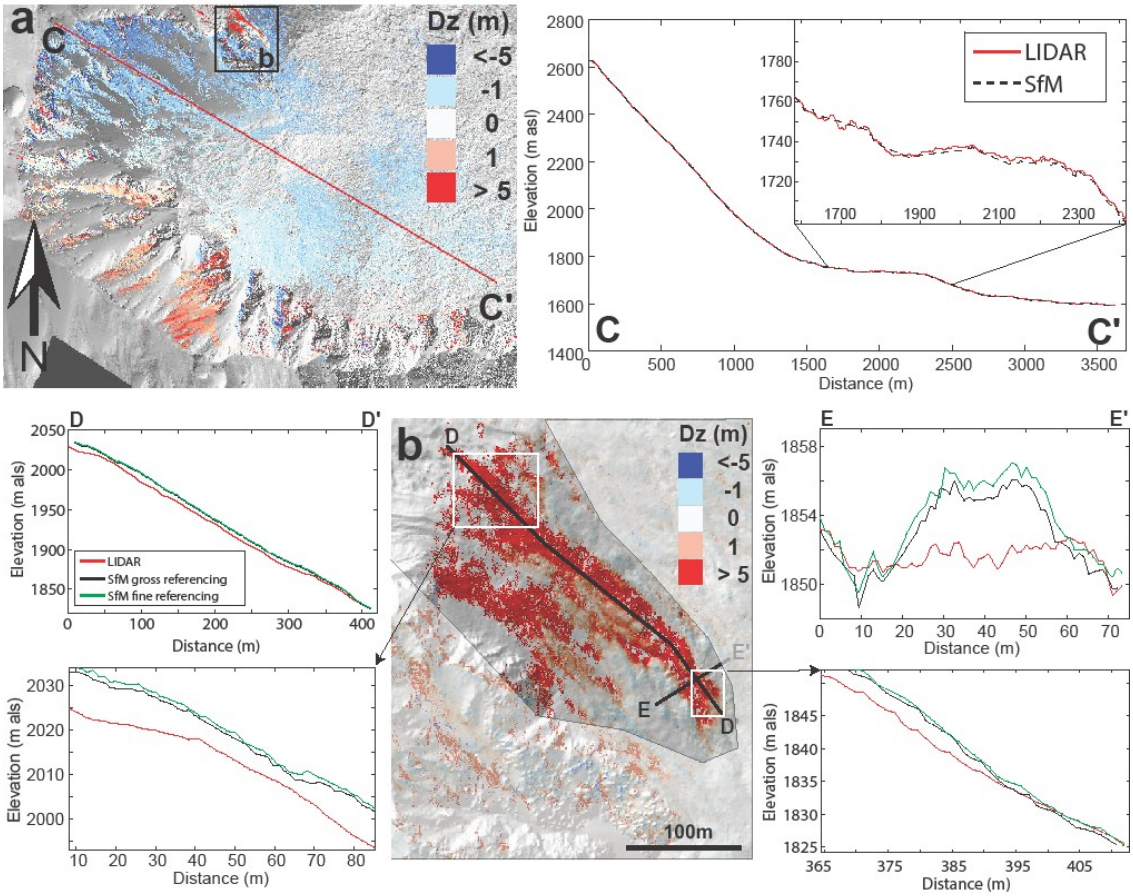

824

Figure 6: Evaluation of the SfM DEM Valle del Bove.

826a) Vertical error between the SfM and the LIDAR data overlain on the hill-shaded LIDAR DEM. The profile line has a length of 3.65 km. Note the large "data shadows" in the SfM
828model, resulting from the low vantage point of image acquisition. The profile A-A' shows the striking agreement between LIDAR and SfM data in spite of the large data shadows. This
830lack of data becomes apparent in the zoom in of profile A-A', where the LIDAR data shows higher spatial detail. However, the interpolated SfM data matches the LIDAR data to within
8323 m. b) Detail of the SfM data showing lava flows emplaced from February to March 2013 in the area of interest in the northern section. The area used during the second georeferencing
834step (i.e. the non-masked area) is highlighted by the pale overlay. Profiles B-B' and C-C' show longitudinal and transversal sections of this flow, respectively. Plotted are the LIDAR
836data in red; the SfM data geo-referenced to the entire Valle del Bove DEM; and the SfM data geo-referenced to a DEM for which the lava flow sections were masked. Profile sections
838from within the two white boxes are enlarged for detail. Note the improved vertical accuracy of the re-referenced dataset.
840

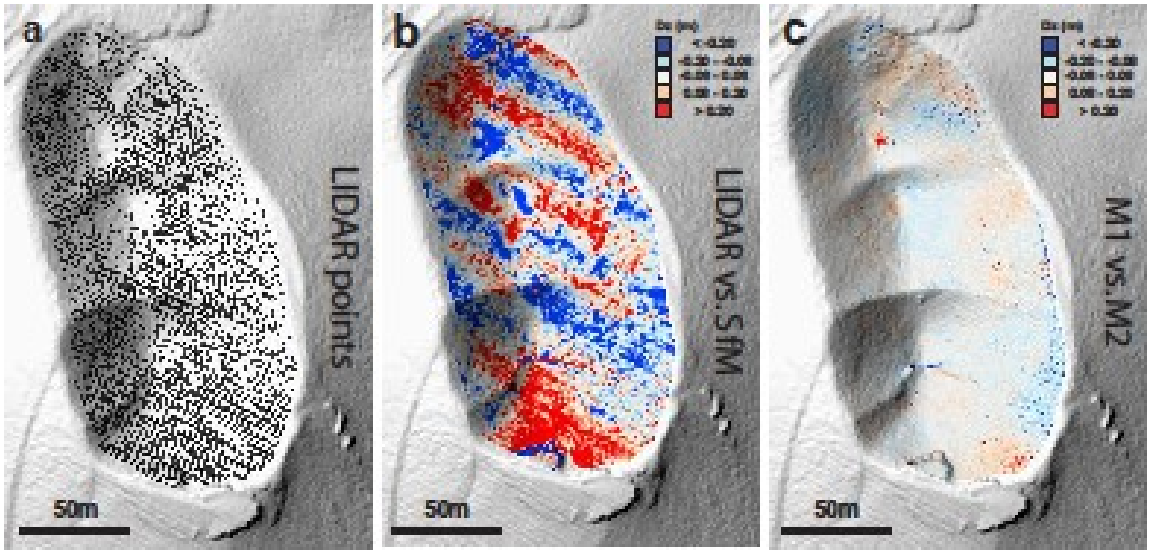

Figure 7: LIDAR and SfM error mapping

a) LIDAR point distribution in the study area. Linear point arrangement is a result of the scanning motion of the LIDAR sensor. Note the lack of data in the center of all three craters, resulting in an overestimation of the altitude through interpolation during DEM creation b) Vertical difference (Dz) between LIDAR DEM and SfM DEM. c) Vertical difference (Dz) between M1 and M2 (two DEMs created from independent image datasets using the methodology described in this manuscript). Both b and c are mapped at 0.5 m grid step. The red area in the northern end of the Monti Silvestri superiore feature is a result of a lack of data in one of the DEMs in this location.

40

856

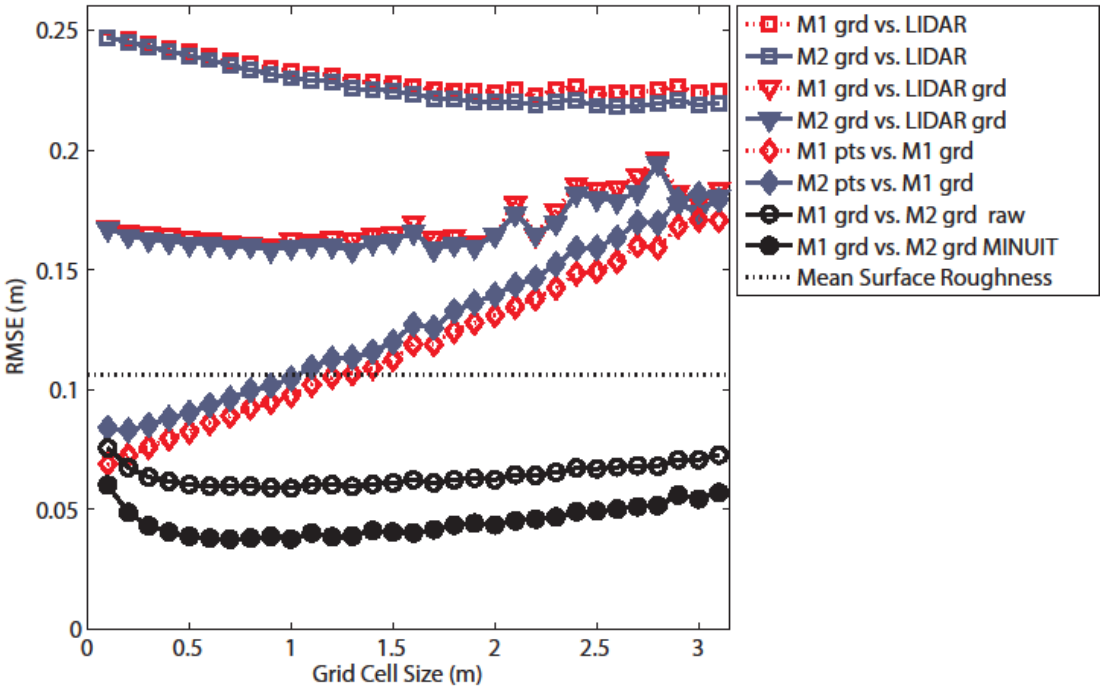

858

Figure 8: Evaluation of the effect of grid cell size on RMSE of the reconstruction.

860 Empty and filled squares represent the M1 and M2 datasets compared to the LIDAR data (at 0.5 m grid step). They show an overall decreasing RMSE with increasing grid size. The 862 RMSE between the gridded DEMs derived from SfM and LIDAR drops by 0.04-0.08 m when comparing the M1 and M2 datasets (empty and filled triangles, respectively) with the 864 LIDAR data gridded at the same respective grid sizes. When comparing the two gridded models, after having been generated independently through the workflow presented here, to 866 each other (empty black circles) we recover very low RMSE values that first decrease with increasing grid size, reaching a minimum at 0.6 m cell size and then gradually increase again 868 towards larger grid sizes. The same effect is observed, in an even more pronounced manner, when evaluating the self-similarity of the two independent datasets by making them undergo 870 a further MINUIT guided error minimization (filled circles).

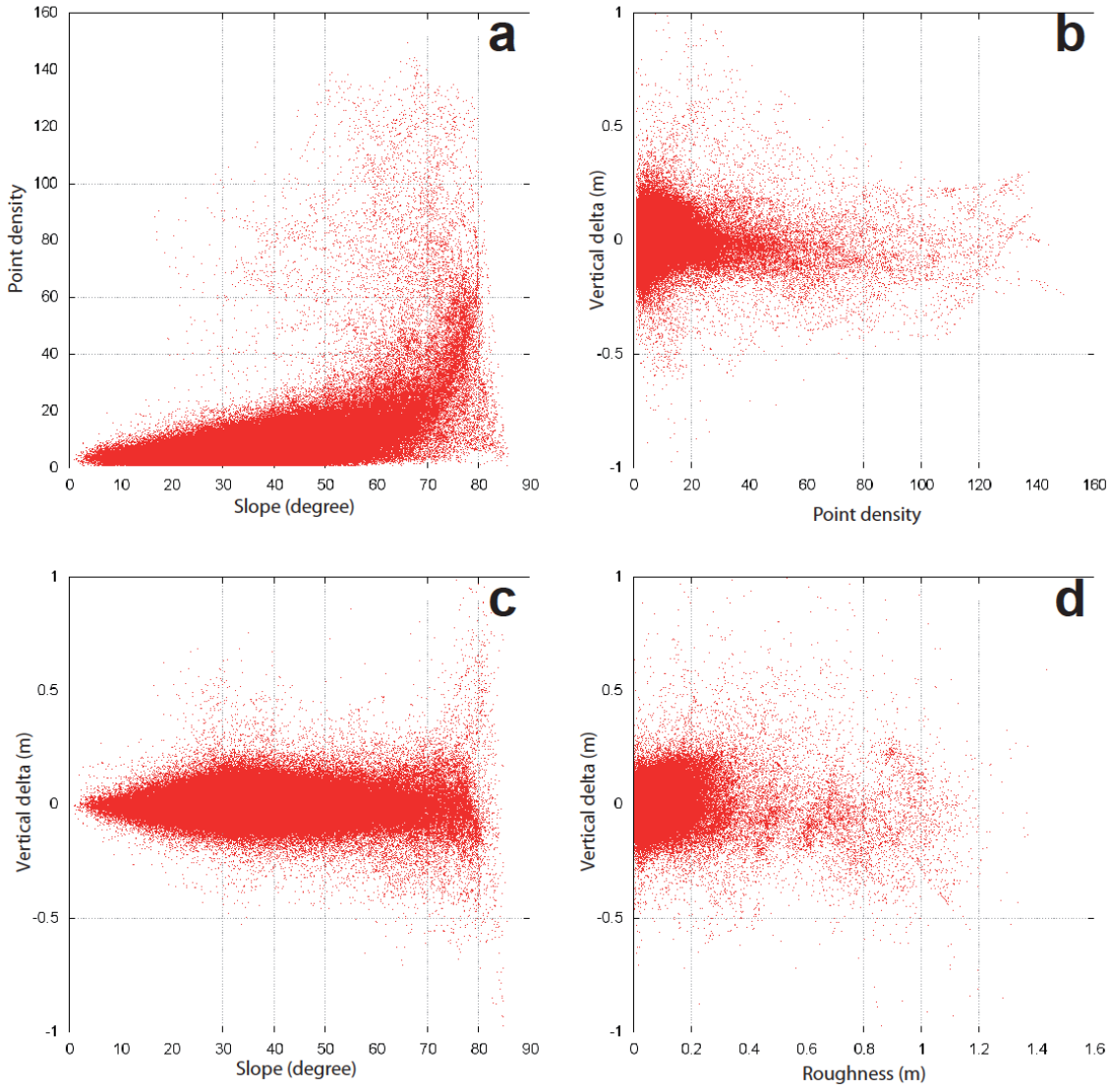

Figure 9: SfM model statistics:

a) Plot showing the point density (in points per pixel at 0.5m pixel length) at the respective slope angle for the model Monti Silvestri superiore. There is a quasi linear increase in point density with increasing slope angle for angles below 40 degrees. At slopes steeper than 40 degrees there is a nonlinear increase in point density with increasing slope. b) Plot of the vertical difference between the SfM and LIDAR DEM as a function of point density (in points per pixel at 0.5 m pixel length). There is an overall decrease in the vertical difference with increasing point density. c) Plot of the vertical difference between the SfM and LIDAR DEM as a function of the slope of the surface. Between 0 and 30 degrees, the data show a linear increase in RMSE with increasing slope. Between 30 and 70 degrees the vertical difference reaches a more or less steady value around 0.229. At slopes steeper than 70 degrees the RMSE increases drastically and the total number of reconstructed points becomes scarce. d) Plot of the vertical difference between the SfM and LIDAR DEM as a function of the surface roughness of the SfM DEM (i.e. the standard deviation between the points in a

42

grid cell and the averaged grid cell value). Few parts of the SfM model have a roughness greater than 0.4m and there is no systematic relationship between the vertical difference and the model's surface roughness.

	covered area (m^2)	longest mod axis (m)
Cono doppio	24,626	230

TABLE I
OVERVIEW OF SURFACE MODEL CHARACTERISTICS

44